Chapter 5

PWR migration: application to field data

5.1 Introduction

The plane-wave-response migration method described in chapter 4 was applied to a marine dataset from Petrobras, recorded off the eastern coast of Brazil. Preparing the data for the migration involved a few processing operations which conditioned the data according to the restrictions and assumptions imposed by the migration/modeling scheme, such as frequency content and 2-D simulation. The elastic background model was constructed using integrated information from well-logs, seismic data, and geologic knowledge of the area. The memory-bound limitations discussed in chapter 4 restricted not only the angular coverage and resolution of the plane-wave decomposition, but also the shotpoint coverage of the final image-cube. Even the small angular coverage used (24 angle intervals of 15 degrees) required the exclusive allocation of our CM2 parallel computer. Despite the exceptional patience of other users with my abusive use of the machine, I restricted myself to migrate only every eighth shotpoint. Although the resolution of the final image-cube was strongly affected by these limitations many consistent events can be observed. Surprisingly, a fault-plane not observed in the scalar migration was imaged at low incidence angles.

5.2 Data description and construction of the background model

5.2.1 Data description

The seismic line where the migration was applied is part of a 3-D survey that covers a transition zone at the margin of the continental shelf. The lithology is characterized mainly by limestones interbedded with marls, with some occurrence of turbiditic deposits and shales. Most of the carbonates have grain sizes represented by calcilutites and calcisiltites. The sedimentary process involved different phases which include evaporative (bottom), restricted shelf, open platform, and open shelf.

The exploration targets are characterized by hydrocarbon accumulations associated with stratigraphic traps, mainly of turbiditic origin. The stratigraphic nature of these reservoirs instigate the use of data-processing technologies that go beyond the structural imaging of the subsurface. Bright spots and AVO analysis have been used in the area with some success, but the use of more refined inversion techniques can improve the resolution and help the interpreter in cases for which standard direct-indicators have failed.

Figure 5.1 shows a migrated section corresponding to the part of the data that was used to test the plane-wave-response migration method. Although the line is part of a 3-D survey, the section in Figure 5.1 represents a simple 2-D post-stack migration.

Figure 5.2 shows a common-shot gather corresponding to a source positioned 1250 meters from the origin. The cable extends for about 3.12 Km to the right of the source. The data has been resampled from the original 2 milliseconds to 4 milliseconds to reduce the migration processing time.

5.2.2 Borehole information

Several borehole logs from a well located 5000 meters from the origin in Figure 5.1 were available on both paper and tape. The sonic log (shown in Figure 5.3 covered the depth interval from 900 to 3400 meters. The density log, however, was recorded only at depth intervals from 2445 to 2985 meters and from 3080 to 3400 meters. Using these two overlapping windows between the sonic and density logs, I estimated the parameters for the fitting function

$$\rho = (a + bz)\, v_p^{\alpha},$$

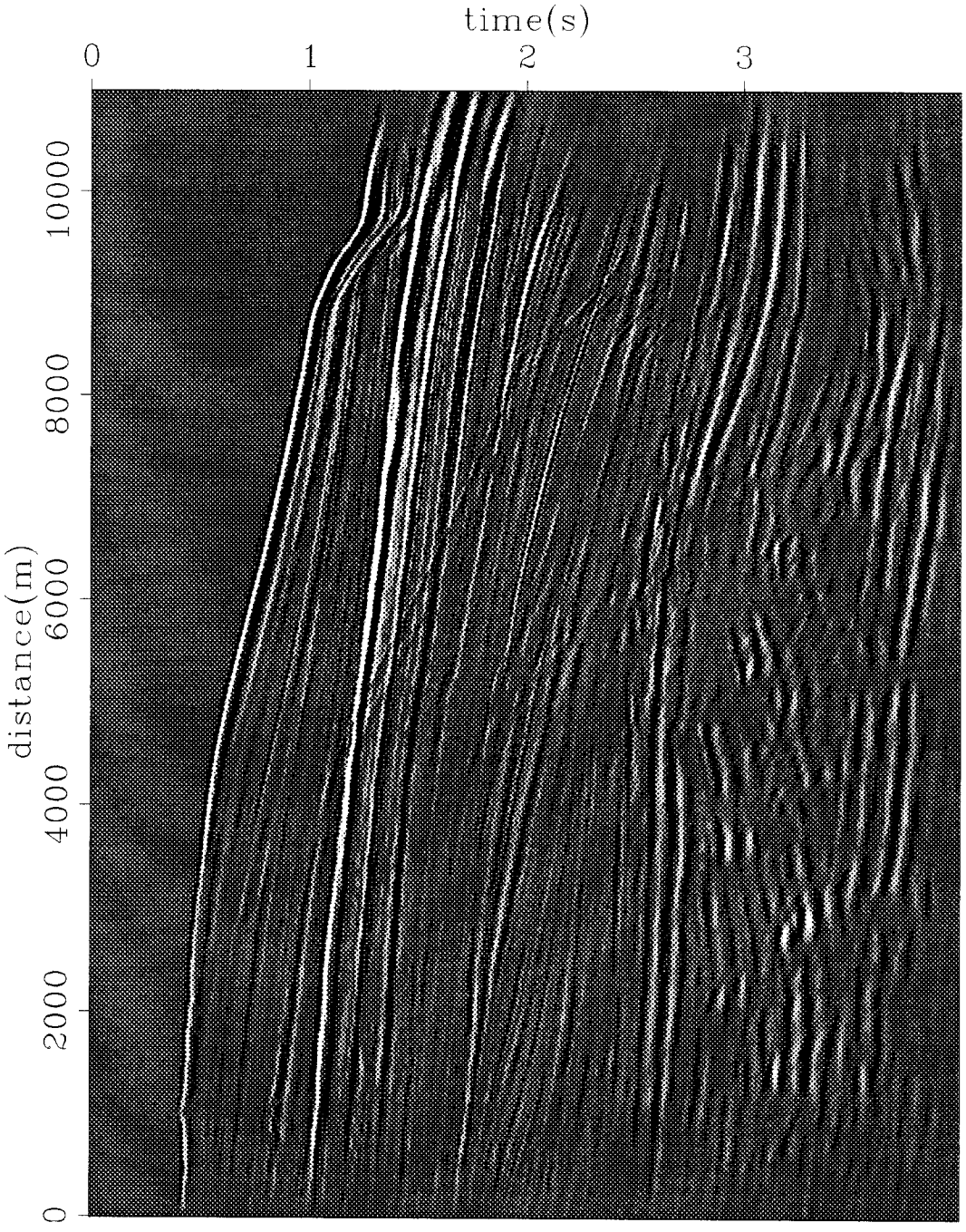

FIG. 5.1. Migrated (post-stack) seismic line from Brazil offshore. The survey was conducted from the right to the left with water depths ranging from 75 meters to more than 1Km over the complete line (only the central part is shown). Minimum and maximum source-receiver offsets are 146 and 3121 meters, respectively, with 25 meters interval. The distance between successive shots is also 25 meters.

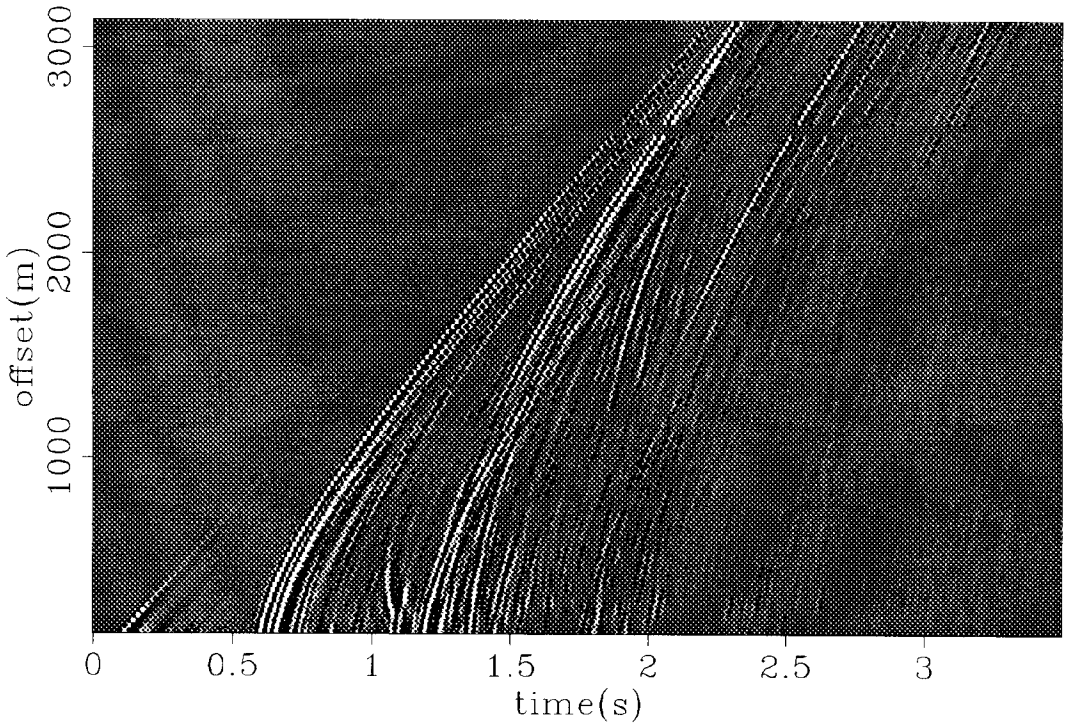

FIG. 5.2. A shot gather from the line shown in Figure 5.1. A balance factor proportional to the time was applied to simulate acquisition in a 2-D world with linearly-increasing velocity with depth. This simulation is only partial because no phase correction has been applied.

where ρ is the density in grams per cubic centimeter, z is the depth in meters, v_p is the compressional velocity in meters per second derived from the sonic-log, and a, b and α are the fitting parameters. The estimated fitting parameters are $a = 0.211$, $b = 7^{-5}$, and $\alpha = 0.22$.

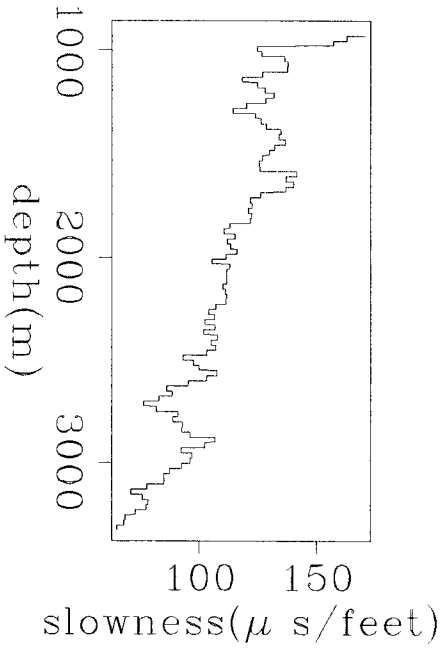

FIG. 5.3. Sonic log near the 5000 meter horizontal position in Figure 5.1. Walsh-spectrum decomposition and filtering were applied to the log to emphasize the layered structure.

An S-wave velocity profile was also obtained from the sonic log using Wyllie's time-average equations (Wyllie et al., 1956) for both P and S wave types with parameters defined by the average lithology of the area, as follows:

$$t_s = (t_p - t_{map}) \frac{(t_{fs} - t_{mas})}{(t_{fp} - t_{map})} + t_{mas},$$

where t_p is the P wave slowness obtained from the sonic log, t_s is the estimated S wave slowness, t_{map} and t_{mas} are the P and S slownesses in the matrix rock, and t_{fp} and t_{fs} are the P and S "slownesses" in the percolating fluid. Although a fluid "slowness" for S waves does not make sense in physical terms, values in the range of 300-500 milliseconds per foot will give acceptable values for t_s in most lithologies (Schlumberger log-interpretation charts, 1989).

To fill the gap in the shallow depths of the sonic-log, I used information provided by the stacking velocity analysis and reflector slopes measured in the migrated section. The

stacking velocities picked from the semblance panel were first corrected for slope using the relation

$$\frac{\tan\theta}{V_{\text{stack}}\,\cos\theta} = \frac{\partial t}{\partial x}, \tag{5.1}$$

where θ is the reflector's dip angle, $\partial t/\partial x$ the slope measured at the migrated section, and V_{stack} the picked stacking velocity. Equation (5.1) is solved for θ, which is the used to obtain the dip corrected RMS velocity

$$V_{RMS} = V_{\text{stack}}\,\cos\theta,$$

Figure 5.4 shows a contour plot of the semblance velocity analysis at the common midpoint gather located at the same position as the well-logs. Two curves are overlaid on the contour panel: the continuous line represents the interval velocity log obtained by the procedure described above, and the dashed line curve represents the "stacking" velocity derived from the interval velocities, including the dipping factor $1/\cos\theta$.

Figure 5.5 shows the three estimated logs used to generate the background model. A Walsh decomposition and filtering (Lanning and Johnson, 1983; Cunha, 1991) was applied to these logs to obtain a coarser version of the logs that fits the model grid-cell size without the smoothing effect of simple slowness averaging.

5.2.3 Construction of the background model

Factors that influenced the determination of the gridding parameters include the migration processing time, available memory in the data parallel unit (DPU), stability conditions and numerical dispersion in the finite-difference schemes, data-acquisition parameters, and propagation velocity range. The grid dimensions are 372 cells in the horizontal direction and 144 in the vertical direction. The cell size is 25×25 meters.

The building of the model involved the integration of the velocity-density logs of Figure 5.5 with structural information obtained by manual picking of the representative interfaces in the migrated section. A total of six interfaces sampled at nine surface locations was picked with additional measuring of the interfaces slopes at the right and left boundaries of the model.

The model is obtained in three steps:

- The depths where each of the representative interfaces crosses the center (the vertical center line) of each grid is obtained by spline interpolation of the picked points and slopes of each interface.

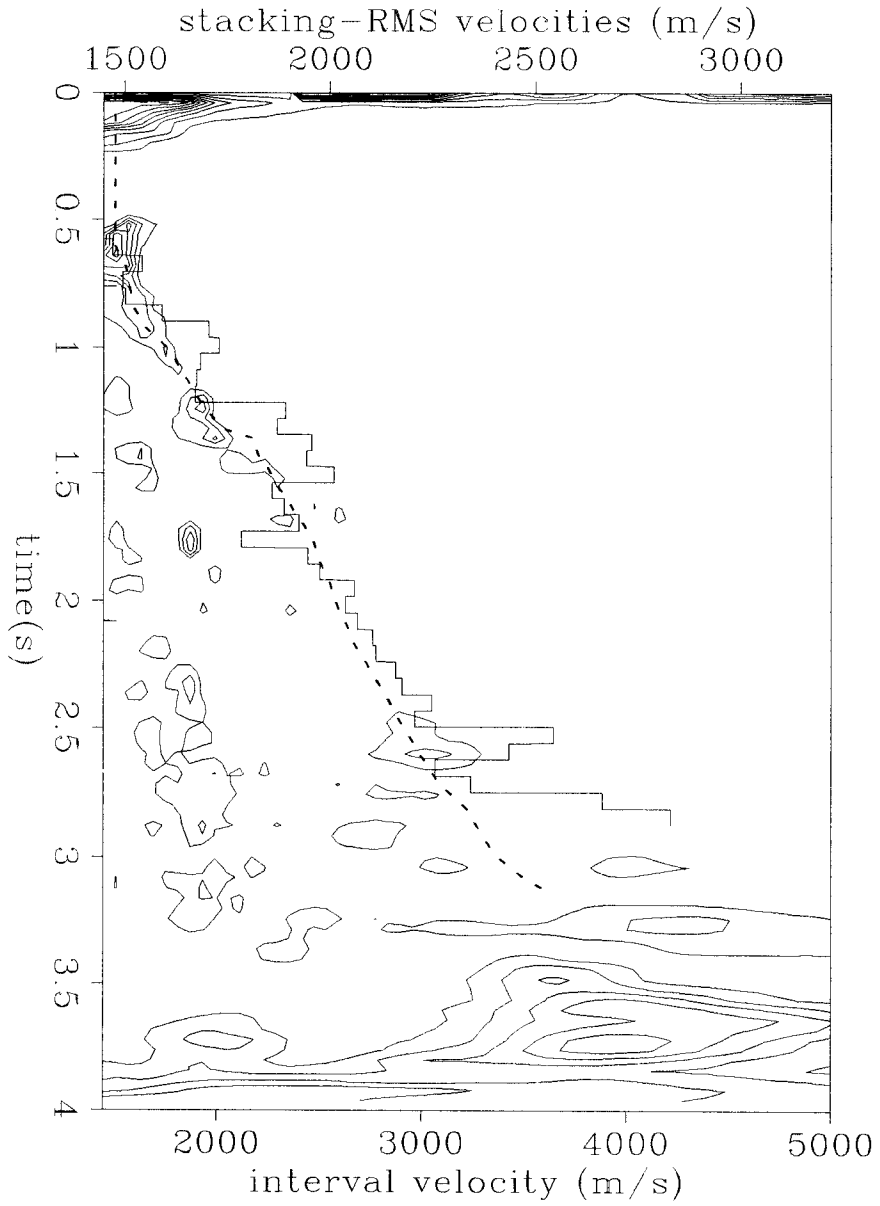

FIG. 5.4. Semblance contours of a stacking velocity analysis at the same location as the logs in Figure 5.5. The two overlaid curves are derived from the sonic log (below 1.2 seconds) and from manual picking of events in the semblance panel (above 1.2 seconds). The continuous line refers to interval velocity (bottom scale) and the dashed line to RMS velocity (upper scale).

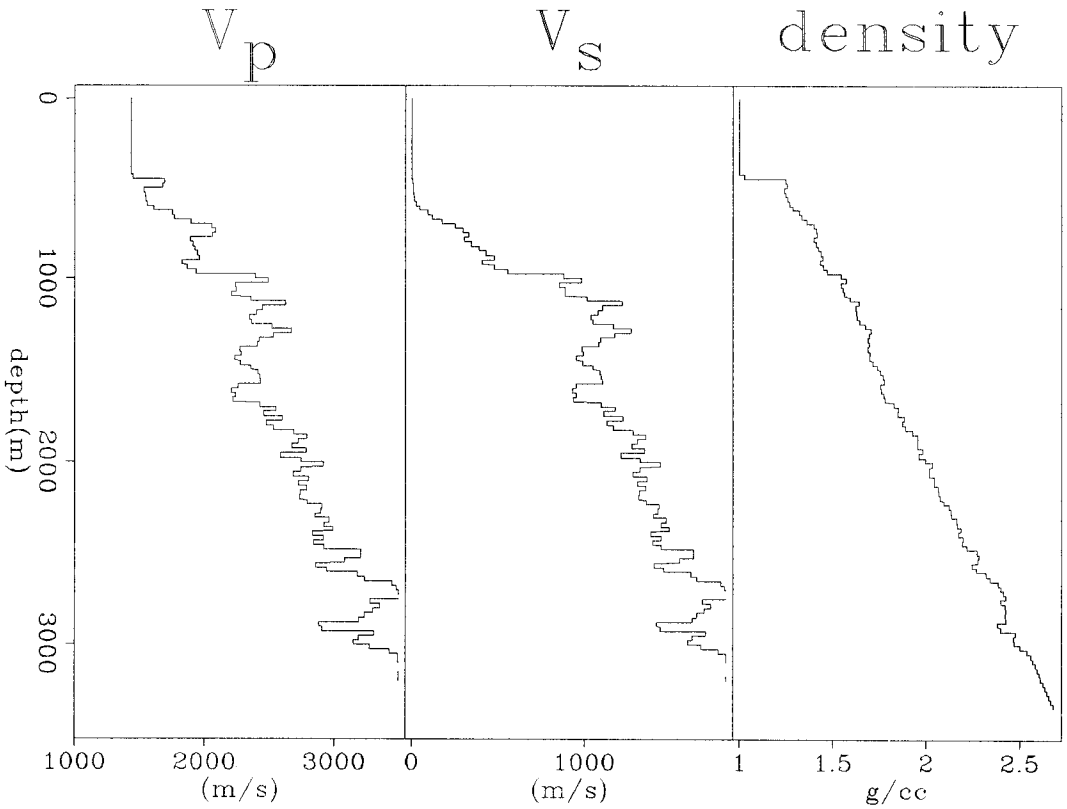

FIG. 5.5. Empirically derived logs for P-wave velocity, S-wave velocity, and density. The density log was obtained by using an empirical relation between the sonic and density logs based on two depth windows for which the actual density log was available.

- Next, assuming a constant average slowness between any two interfaces (which is equivalent to the assumption of laterally homogeneous layers) constant layer-thickness intervals are obtained for each surface position and for each interval between the picked interfaces. The well-location is used as reference with a layer thickness equal to the grid-cell size.

- Finally, the model values at the well location are extended laterally, using Shoemberg-Muir equivalent-media-based interpolation.

Figure 5.6 shows the C_{11} component of the model. The distances labeled on the horizontal axis of Figures 5.1 and 5.6 refer to the same origin.

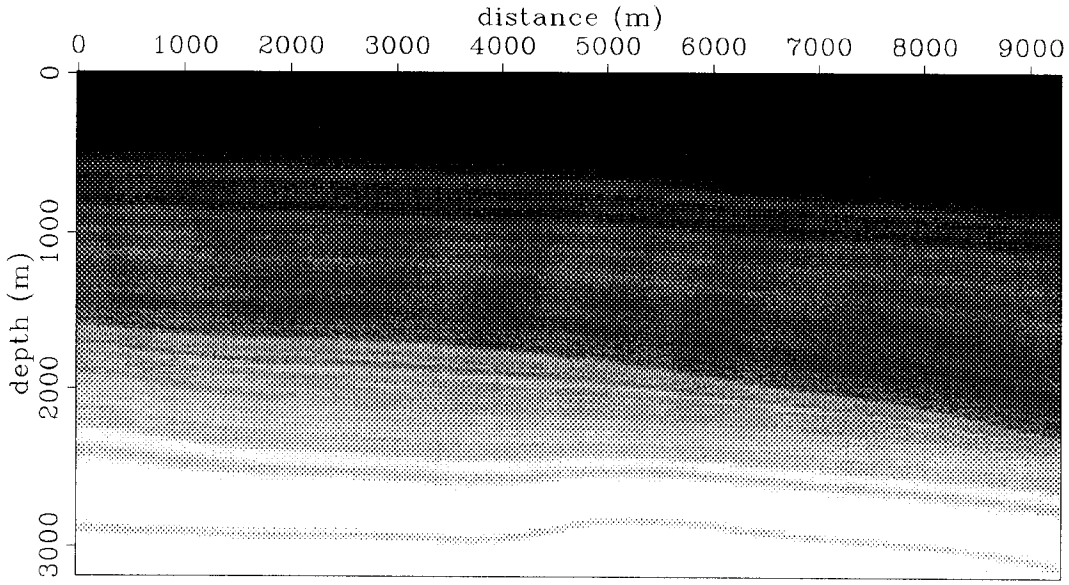

FIG. 5.6. The C_{11} component of the background model corresponding to the data of Figure 5.1. The vertical dimension in the figure has a exaggeration of 1.5 relative to the horizontal dimension. Values range from $2.25 \times 10^6 N/m^2$ (black tone at the top) to $3.3 \times 10^7 N/m^2$ (white tone at the bottom). The background model is isotropic (C_{11}=C_{33}) and was built using integrated information from velocity analysis, well-logs, and the post-stack migrated section.

5.2.4 Testing the model

As with many other inversion methods, it is important that the background model represent a good approximation of the actual model. In particular, the kinematics associated with the background model should not differ from the true kinematics by more than half

the characteristic wavelength. A direct way to test this requirement is to compare the data with synthetic data generated with the background model. Figure 5.7 shows a synthetic shot gather for the same shot-receiver geometry as that of the shot gather shown in Figure 5.9.

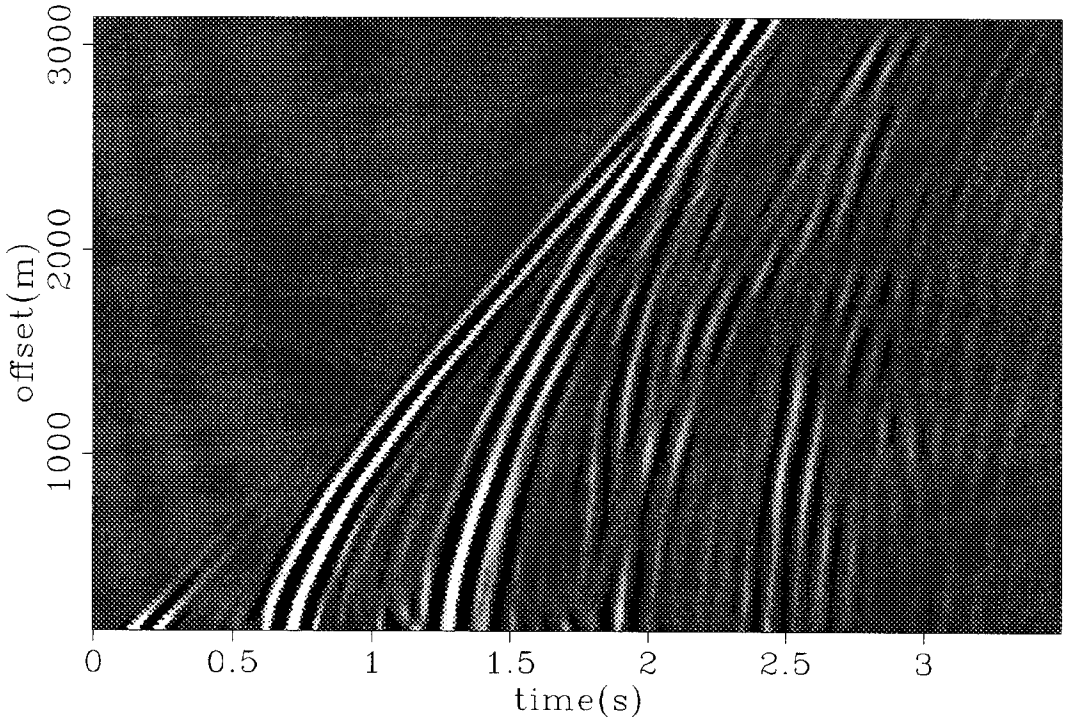

FIG. 5.7. Synthetic pressure wavefield generated by the dual-operator finite-difference scheme using the model shown in Figure 5.6. A source with a fundamental frequency of 14 Hz was used to avoid instability and numerical dispersion. This figure should be compared to the filtered shot gather shown in Figure 5.9.

5.3 Processing and migration of the data

5.3.1 Spectral conditioning and the source radiation pattern

Because of the good quality of the data and because the migration method incorporates the propagation of multiple reflections, the need for data preprocessing was substantially reduced. However one important preprocessing step involves the reshaping of the source/instrument signature. Because of the low-frequency restriction imposed by the choice of the discretization parameters, the model wavelet for the data corresponds to a

low-pass version of the original source signature estimation.

First a shaping-filter, designed according to a least-squares criterion to reduce the instrument signature to a zero-phase low-frequency second-derivative Ricker wavelet (Figure 5.8), was applied to the data. After this deterministic filter, predictive deconvolution was applied to the data to remove the long-period oscillations from the source wavelet. The size of the predictive operator was 448 milliseconds and the prediction lag 224 milliseconds. Figure 5.9 shows the same shot gather as in Figure 5.2 after application of each of these filters.

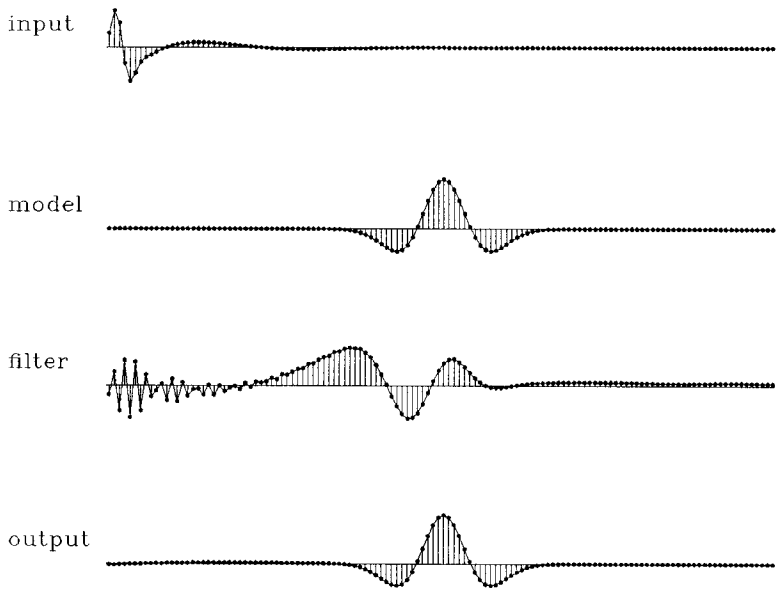

FIG. 5.8. From top to bottom, the first trace (input) is the signature of the recording instrument, the second trace (model) is the desired deconvolved signature, the third trace (filter) is the least-squares estimated filter, and the fourth trace (output) is the result of applying the filter to the first trace.

The radiation pattern of the forward-modeling source term was simulated by using a simple frequency-independent source with elliptical symmetry. The ratio between the horizontal and vertical axes of the ellipse was empirically determined by matching the offset-amplitude-decay of the ocean-floor reflection in the field and synthetic data.

5.3.2 Line-source simulation

The migration method described in chapter 4 was developed using a point-source in a 2-D space that is equivalent to a line-source perpendicular to the survey plane in a 3-D

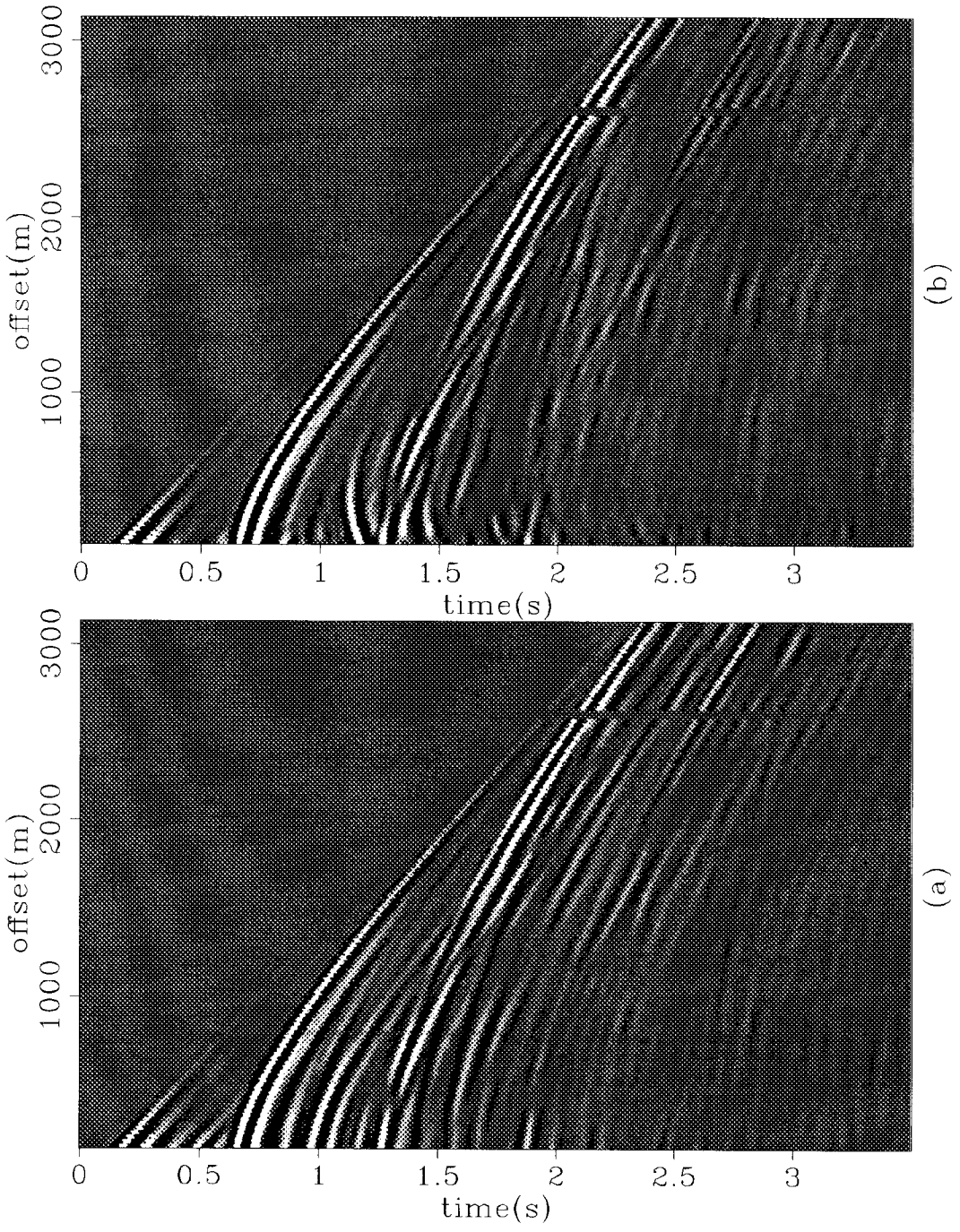

FIG. 5.9. (a) Result of applying the shaping filter of Figure 5.8 to the shot gather shown in Figure 5.2. (b) Result of applying predictive deconvolution to the data in (a). This figure should be compared to the synthetic gather shown in Figure 5.7.

space in which the subsurface structures are invariant along the line-source direction (2-D geology). Wapenaar et al (1990) showed that within the assumption of a 2-D geology, point-source data can be transformed into line-source data by the following integration:

$$\phi(x,t)_{line} = \int_{|x|}^{\infty} \frac{\phi(\rho,t)_{\text{point}}}{\sqrt{1-(x/\rho)^2}}\, d\rho.$$

For a general inhomogeneous 2-D geology, this integration should be carried out in the common midpoint domain.

Instead of using this more elaborated approach, I opted for a more cost-effective approximation that is usually satisfactory when the geology is not complex. This approximation involves a simple rescaling of the data by the factor proportional to the recording time (Mora, 1987). 2-D geometrical spreading in a constant velocity medium differs by $\sqrt{t}$ from the 3-D spreading. Assuming a linear velocity gradient introduces an extra $\sqrt{t}$ factor.

5.3.3 Wavefield decomposition

The data is introduced in the migration as a time-dependent boundary condition to the elastic wavefield. The vectorizer operator described in chapter 2 was applied to the recorded pressure field to generate the required elastic field. Figure 5.10 shows the elastic wavefield corresponding to the the pressure data shown in Figure 5.9.

5.4 Migration results

Figure 5.11 shows some frames of the crosscorrelation cube $\mathcal{C}(x,z,\beta;x_s)$, for a shotpoint located 3150 m from the origin in Figure 5.1. This figure should be compared to Figure 4.13 which represents the same cube for the synthetic data of chapter 4. Each panel corresponds to a different angle of incidence of a plane wave relative to the local reflector normal. Only part of the model is shown in this figure, so that for any panel the source is located near the upper-left corner. There are some important differences from the synthetic-data example mainly because of the reflector's dip to the right. First, it is clear at small angles the leftward trend of the imaging-point as depth increases. Second, the rightward drift of the imaging-points as the angle of incidence increases is slower than for the synthetic case. Although some artifacts (dipping to the right) can be observed, specially at small angles of incidence, they are occasional and unlikely to degrade the imaging after the integration

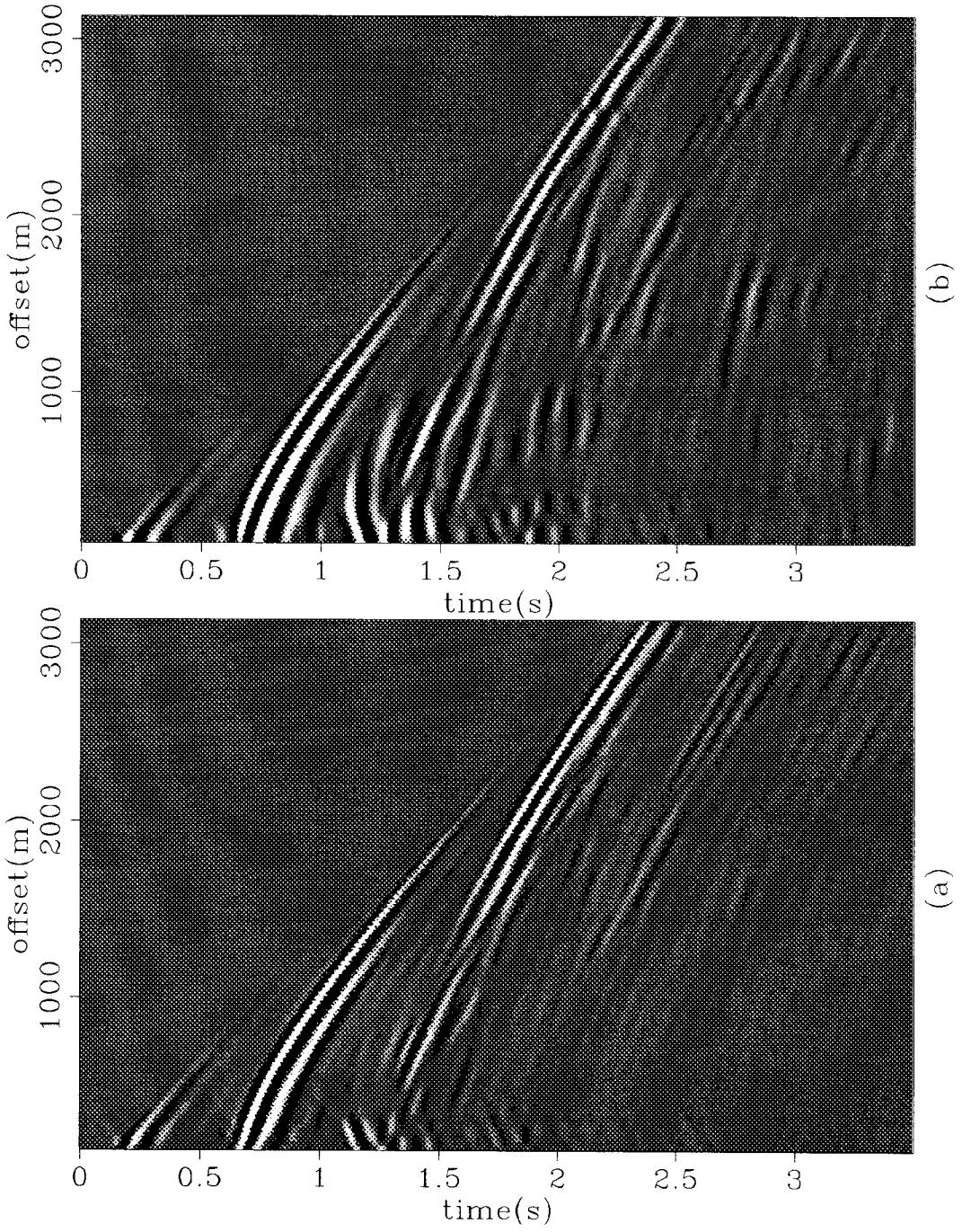

FIG. 5.10. Elastic wavefield decomposition of the pressure wavefield shown in Figure 5.9. (a) Horizontal component of the wavefield. (b) Vertical component of the wavefield.

over shotpoint. As expected the energy and coherence substantially decrease at larger angles of incidence.

Figure 5.12 shows the final PP plane-wave-reflectivity image-cube obtained after the integration over shotpoints. As discussed before, only every eighth shotpoint was migrated to generate these images. The angle resolution in the plane-wave decomposition is 15 degrees. Because of the low converage in both angle and shotpoint these final images have a poor resolution, with the characteristic artifacts (events dipping up to the right) of low coverage crossing the session specially at intermediate angles and side boundaries. However, laterally coherent events can be observed up to 75 degrees with predominance of deep events at small angles and shallow events at large angles. As expected, the image corresponding to 82.5 degrees is much weaker and less coherent than the others.Two events deserve special attention: the strong, shallow, flat event at 67.5 degrees, and the event dipping down to the right at the center of the 15 degree-image. The former would be a good candidate for Zoeppritz inversion except for the fact that it is located at the boundary where the coverage even lower. The latter appears to be the imaging of a fault plane. The fault is apparent in the middle of Figure 5.1 because of the vertical shift in several reflectors but the fault plane is not visible in this figure.

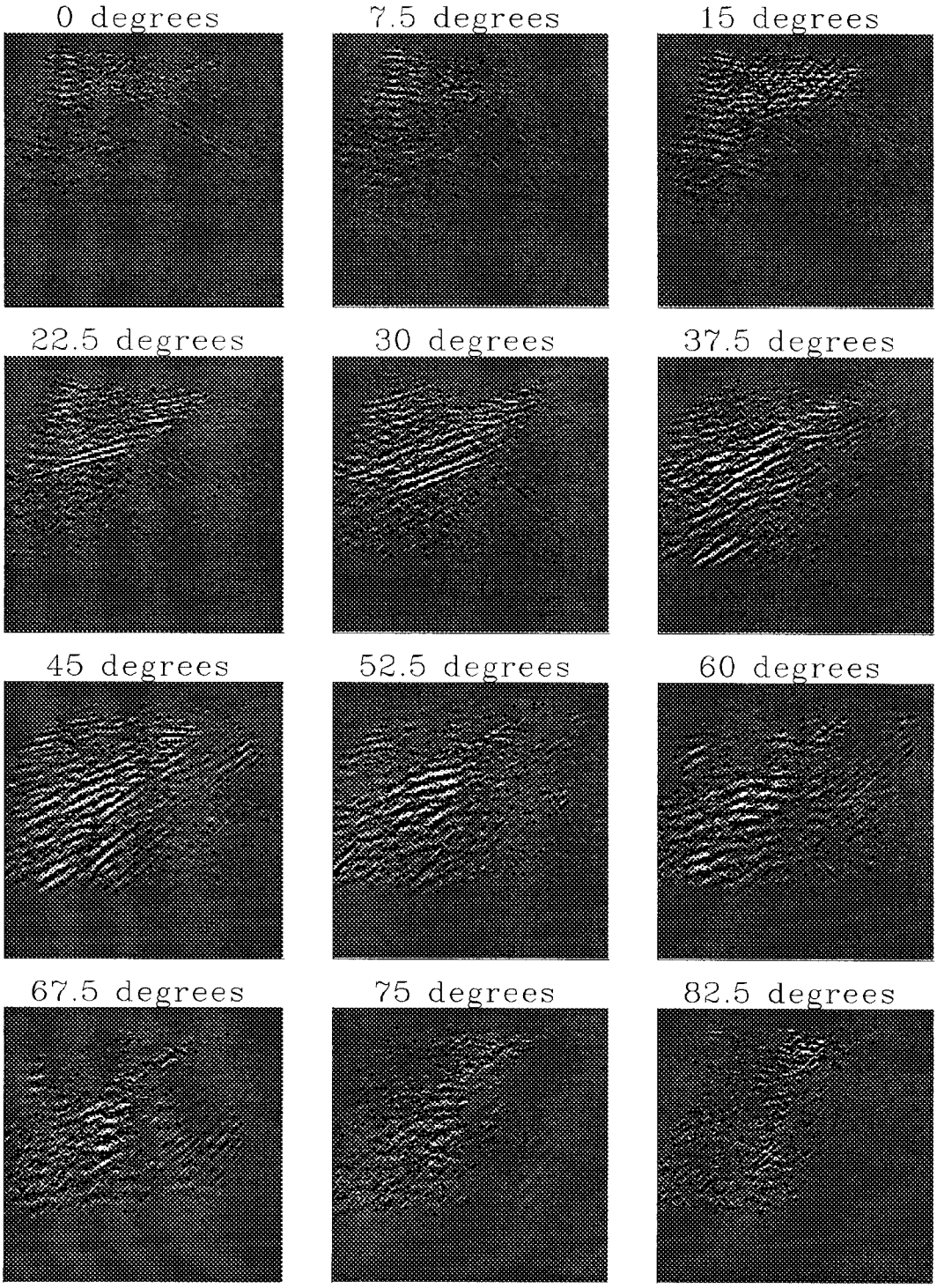

FIG. 5.11. PP crosscorrelation cube (for a shotpoint located 3150 m from the origin in Figure 5.1).

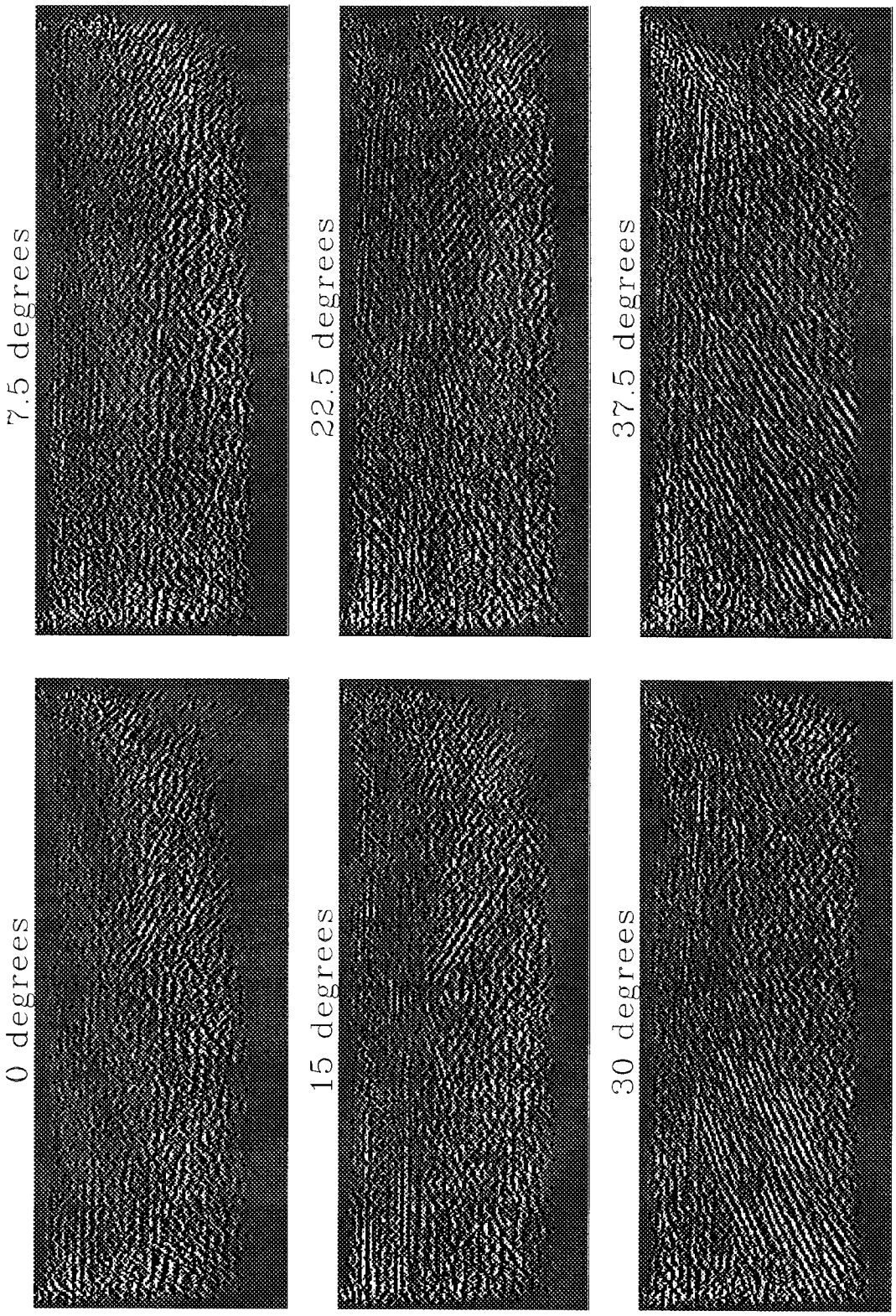

FIG. 5.12. PP plane-wave-reflectivity cube.

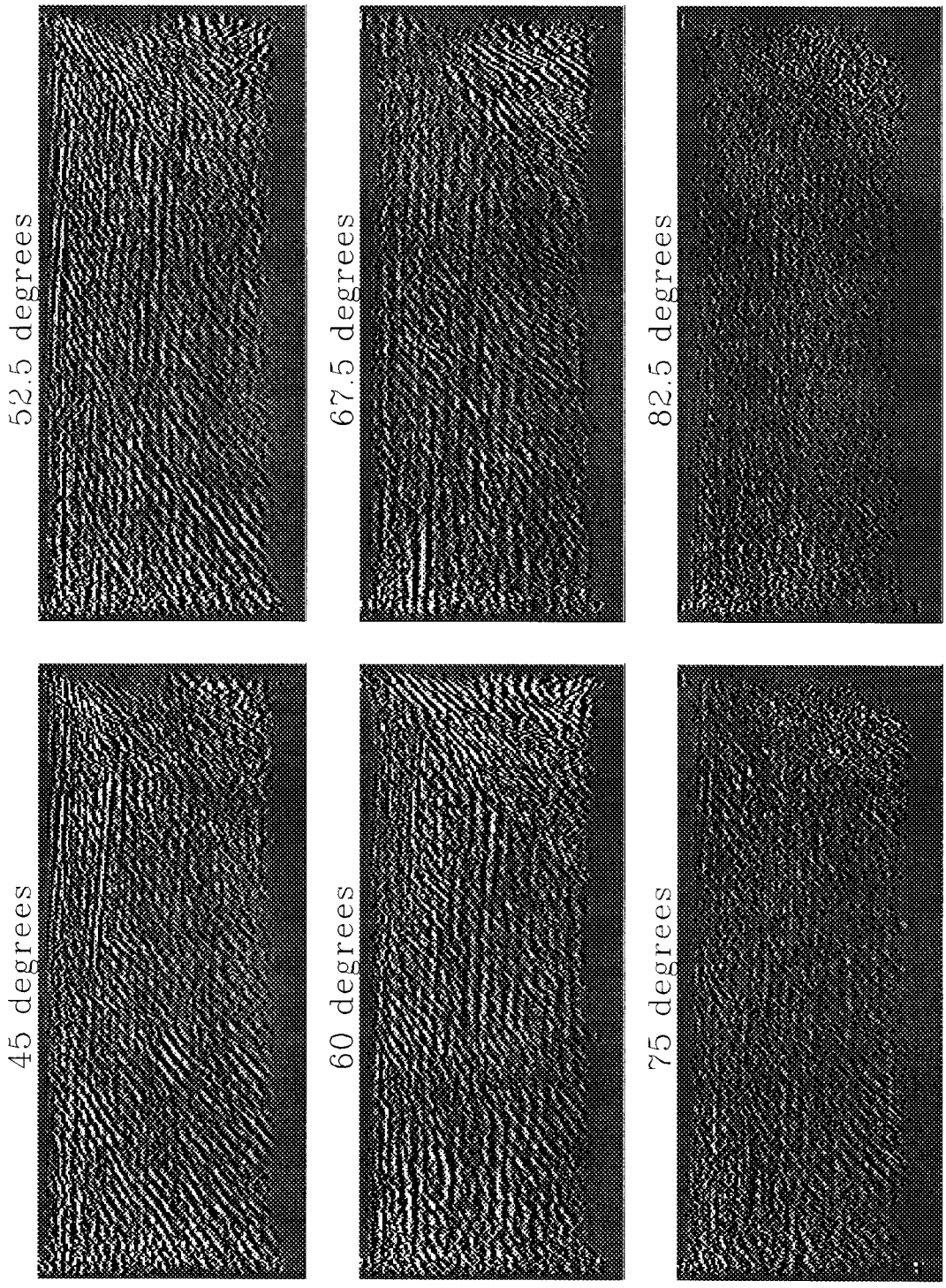
45 degrees
52.5 degrees
60 degrees
67.5 degrees
75 degrees
82.5 degrees